catalysts

MDPI

Article

Effect of the Preparation Method on Cu-MOR/g-C_3N_4 for Direct Methanol Synthesis from Methane Oxidation by Photothermal Catalysis

Jun-Cai Hao [1,2], Rui-Xin Zhang [3,4], Miao Ren [3,4], Jia-Xuan Zhao [5], Zhi-Hua Gao [3,4], Lei Liu [4], Zhu-Xia Zhang [1,2,*] and Zhi-Jun Zuo [3,4,*]

1 College of Chemistry, Taiyuan University of Technology, Taiyuan 030024, China; juncai_hao@163.com
2 College of Materials Science and Engineering, Taiyuan University of Technology, Taiyuan 030024, China
3 State Key Laboratory of Clean and Efficient Coal Utilization, Taiyuan University of Technology, Taiyuan 030024, China; zhangruixin0659@link.tyut.edu.cn (R.-X.Z.); renmiao_happy@126.com (M.R.); gaozhihua@tyut.edu.cn (Z.-H.G.)
4 College of Chemical Engineering and Technology, Taiyuan University of Technology, Taiyuan 030024, China; liulei@tyut.edu.cn
5 College of Software, Taiyuan University of Technology, Taiyuan 030024, China; zhaojiaxuan5642@link.tyut.edu.cn
* Correspondence: zhangzhuxia@tyut.edu.cn (Z.-X.Z.); zuozhijun@tyut.edu.cn (Z.-J.Z.)

Abstract: Copper-based zeolite catalysts are widely used in methanol synthesis from methane oxidation, but their photothermal catalytic properties have seldom been explored. This study examines the effect of the preparation method on Cu-based zeolite composite graphite-phase carbon nitride catalysts (Cu-MOR/g-C_3N_4) for direct methanol synthesis from methane oxidation by photothermal catalysis. Four different preparation methods are employed: liquid phase ion exchange (Cu-MOR/g-C_3N_4-IE), isovolumetric impregnation (Cu-MOR/g-C_3N_4-IM), solid-state ion exchange (Cu-MOR/g-C_3N_4-GR), and hydrothermal synthesis (Cu-MOR/g-C_3N_4-HT). Cu-MOR/g-C_3N_4-IE shows the highest methanol yield (3.09 μmol h^{-1} $g_{cat}{}^{-1}$) due to strong interactions between the Cu_xO_y species and g-C_3N_4, as well as smaller interfacial charge transfer forces. This study provides a new method for the design and synthesis of catalysts for the conversion of methane.

Keywords: Cu-MOR/g-C_3N_4; methane; methanol; photothermal catalysis; preparation method

Citation: Hao, J.-C.; Zhang, R.-X.; Ren, M.; Zhao, J.-X.; Gao, Z.-H.; Liu, L.; Zhang, Z.-X.; Zuo, Z.-J. Effect of the Preparation Method on Cu-MOR/g-C_3N_4 for Direct Methanol Synthesis from Methane Oxidation by Photothermal Catalysis. *Catalysts* **2023**, *13*, 868. https://doi.org/10.3390/catal13050868

Academic Editor: Valeria La Parola

Received: 28 March 2023
Revised: 2 May 2023
Accepted: 3 May 2023
Published: 10 May 2023

1. Introduction

Methane is a valuable fossil resource, widely available in natural gas, coalbed methane, shale gas, and methane hydrates [1–4]. Methanol synthesis from methane is a promising method that efficiently utilizes natural gas and produces valuable chemicals [5]. However, the conventional method of methanol synthesis involves indirect generation through syngas, which is a complex process requiring high temperature and pressure and results in energy waste [6]. Therefore, researchers have been working to develop a direct methane oxidation method that can synthesize methanol through a new reaction process or catalyst at lower temperatures. However, this method faces two major challenges: first, the high dissociation energy of 435 KJ/mol is required for the C-H bond of methane [7], and second, the kinetics of selective oxidation of methane to methanol is slower than the over-oxidation of methanol [8]. On the other hand, the selective oxidation of methane to methanol is kinetically slower than the over-oxidation of methanol. Therefore, finding a new reaction process or catalyst to achieve methane oxidation in methanol synthesis is of great significance.

Inspired by the natural methane monooxygenase (MMO), some researchers study methane oxidation at low temperatures (<200 °C) on iron-cobalt or copper-loaded zeolites with O_2 or N_2O as the oxidant [9]. This is because they have similar metal-oxo structures

and methane activation mechanisms to the MMO enzyme systems [10]. Among these catalysts, copper-based zeolite (eg. zeolites, MOR and SSZ-13) catalysts are currently the most excellent catalysts with O_2 as the oxidant [11–14]. It is generally accepted that small Cu_xO_y species confined in molecular-sized micropores are the active center of the reaction. The 8-membered ring of mercerized zeolite (H-MOR) has a high concentration of skeletal Al, and the Cu species generated after ion exchange not only achieve their uniform distribution but also achieve a high concentration of these sites, leading to higher catalytic activity. At the same time, the 8-membered ring structure of H-MOR provides suitable conditions for the stable presence of the active Cu species [13]. The 8-membered ring structure of H-MOR is similar to the hydrophobic cavity of pMMO and enables the stable presence of active Cu species [15].

Graphite-phase carbon nitride (g-C_3N_4) is a desirable catalytic material due to its excellent chemical stability, low raw material cost, and easy synthesis [16]. Cu_2@C_3N_4 has been used as an advanced catalyst for CH_4 oxidation, while copper-dimer catalysts have also demonstrated high selectivity for partial oxidation of methane using hydrogen peroxide and oxygen as oxidants under both thermo- and photocatalytic reaction conditions [17]. Furthermore, Cu-P-g-C_3N_4 and Au/Pd/gC_3N_4NTs have shown excellent CO conversion efficiency during CO oxidation using oxygen as the oxidizer [18,19].

Most studies of methanol synthesis from methane oxidation involve a multistep process. Typically, the process requires the introduction of O_2 or N_2O at high temperatures for activation, followed by the introduction of CH_4 at low temperatures to the reactor, and finally the extraction of methanol using water or other solvents [10]. The activation temperature is usually higher than the reaction temperature and extraction temperature (~500 °C vs. ~200 °C). Thus, the reaction is divided into three sections, and it is a stoichiometric reaction. However, in recent years, some researchers have attempted to study direct methanol synthesis from methane oxidation at the same temperature [20,21]. Cu-ZSM-5, Cu-MOR, and Cu-SSZ-13 have been studied as catalysts for this process, resulting in methanol yields of approximately 1.81, 0.85 and 6.05 μmol h^{-1} $g_{cat}{}^{-1}$ with CH_4, H_2O, and O_2 as the feed at 200 °C. The primary source of oxygen for methanol production is H_2O [22]. As the reaction temperature increases, the methanol yields are 7.80 μmol h^{-1} $g_{cat}{}^{-1}$ at 270 °C [21] and 194.52 μmol h^{-1} $g_{cat}{}^{-1}$ at 300 °C on Cu-SSZ-13 [22].

In recent years, researchers have become increasingly interested in novel catalytic methods that combine multiple techniques, including thermal catalysis, photocatalysis, and electrocatalysis. These hybrid approaches offer several benefits, including exploiting the unique strengths of each method and exhibiting a significant synergistic effect [23]. Photothermal catalysis is a novel catalytic method, which is a synergistic coupling of photocatalysis and thermal catalysis [24]. Photothermal catalysis has distinct advantages over a simple linear combination of these two methods, including enhanced performance due to the synergistic effect and improved selectivity in some cases, which inhibits catalyst deactivation [25]. As a result, photothermal catalysis has been widely investigated for a range of chemical reactions, including carbon dioxide reduction, hydrogen production, volatile organic compound degradation, and organic synthesis [26–31]. To effectively convert methane, extensive research has been done by photothermal catalysis in the batch reaction [17]. However, the use of photothermal catalysis in continuous reactions, particularly in direct methanol synthesis from methane oxidation on copper-based zeolites, is currently limited.

Catalyst preparation methodology significantly affects a catalyst's physicochemical and catalytic properties, which can impact its effectiveness in a reaction [32–35]. As an example, synthesizing aluminum-oxide (Al_2O_3) support by modified sol-gel, reflux and hydrothermal method to study Al_2O_3 and potassium iodide Al_2O_3-supported (KI/Al_2O_3) catalytic transesterification of sunflower oil [33]. Given the impact of preparation methodology on catalytic performance, this study aims to investigate the influence of preparation methods on photothermal catalysts' activity. In a fixed-bed reactor, we examined the process of Cu-MOR/g-C_3N_4 photothermal catalytic direct methanol production from methane

at a low temperature using O_2 as the oxidant with a range of different preparation methods for Cu-based zeolite catalysts. The production of methanol via photothermal catalysis is a first-time application of Cu-based zeolite catalysts.

2. Results

The methanol synthesis activity of Cu-MOR/g-C_3N_4 composite catalysts prepared by different methods was compared for photothermal catalytic methanol synthesis from methane oxidation. Figure 1 shows that the methanol yield of the catalysts varies significantly. The methanol yields of the catalysts are in the order: Cu-MOR/g-C_3N_4-IE (3.09 μmol h^{-1} $g_{cat}{}^{-1}$) > Cu-MOR/g-C_3N_4-IM (2.59 μmol h^{-1} $g_{cat}{}^{-1}$) > Cu-MOR/g-C_3N_4-GR (2.45 μmol h^{-1} $g_{cat}{}^{-1}$) > Cu-MOR/g-C_3N_4-HT (1.57 μmol h^{-1} $g_{cat}{}^{-1}$). Therefore, Cu-MOR/g-C_3N_4-IE exhibited the best photothermal catalytic activity. Then, the difference in methanol yield on Cu-MOR/g-C_3N_4 prepared by different methods between photothermal and thermal catalysis is studied (Table 1). It is interesting to note that the methanol yield on the four catalysts by photothermal catalysis is higher than that by thermal catalysis (Figure S1). Therefore, visible light is beneficial to improve the yield of methanol. The photothermal efficiency for methanol yield on the four catalysts is in the following: Cu-MOR/g-C_3N_4-IE (25.9%) > Cu-MOR/g-C_3N_4-IM (23.3%) > Cu-MOR/g-C_3N_4-GR (17.5.%) > Cu-MOR/g-C_3N_4-HT (4.02%), and Cu-MOR/g-C_3N_4-IE has the highest photothermal catalytic synergistic effect. The stability test shows that the methanol yield on the four Cu-MOR/g-C_3N_4 catalysts did not change significantly during the 9-hour duration of the photothermal and thermal catalysis reaction, indicating that the catalysts are stable under both conditions.

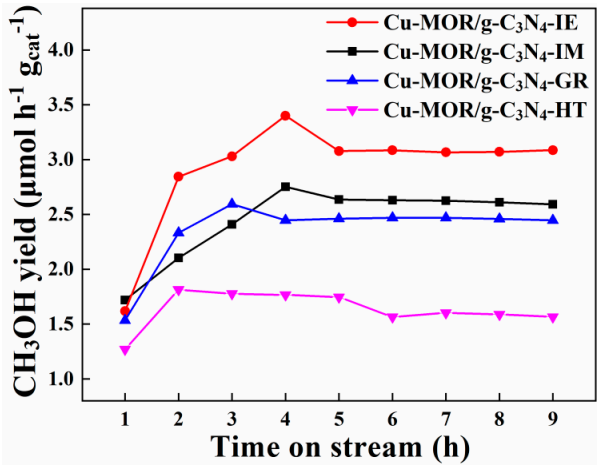

Figure 1. Methanol yield of Cu-MOR/g-C_3N_4 prepared by different methods of photothermal catalysis.

Table 1. Methanol yield of Cu-MOR/g-C_3N_4 with different preparation methods under photothermal catalysis and thermal catalysis.

	Methanol Yield (μmol h^{-1} $g_{cat}{}^{-1}$)		Percentage
	Photo-Thermal	Thermal	
Cu-MOR/g-C_3N_4-IE	3.09	2.45	26.1%
Cu-MOR/g-C_3N_4-IM	2.59	2.10	23.3%
Cu-MOR/g-C_3N_4-GR	2.45	2.00	22.5%
Cu-MOR/g-C_3N_4-HT	1.57	1.50	4.67%

Further investigation revealed that no catalytic activity was observed on Cu-MOR/g-C_3N_4-IE by photocatalysis (Figure S2), suggesting that methanol synthesis on Cu-MOR/g-C_3N4 is a photothermal reaction. Moreover, the methanol yields on Cu-MOR/g-C_3N_4-IE, Cu-MOR/g-C_3N_4-IM, Cu-MOR/g-C_3N_4-GR and Cu-MOR/g-C_3N_4-HT after 9 h reaction are 1.67, 1.61, 1.59 and 1.42 μmol h^{-1} $g_{cat}{}^{-1}$ by thermal catalysis (Figure S3).

Methanol yields on Cu-MOR/g-C_3N_4 are higher than that on Cu-MOR by thermal catalysis. In contrast, Cu-MOR did not exhibit photocatalysis activity for methanol synthesis (Figure S4), suggesting that g-C_3N_4 plays a crucial role in facilitating methanol production under photothermal catalysis. The reason is that C_3N_4 reduces O_2 to $\cdot O_2^-$, and $\cdot O_2^-$ transfers from carbon nitride to Cu_xO_{y-1} (eg. Cu_3O_2) [36]. Since the oxidation ability of $\cdot O_2^-$ is greater than that of O_2, the formation rate of Cu_3O_3 species using $\cdot O_2^-$ as the oxidant is greater than that of Cu_3O_3 species using O_2 as the oxidant. As a result, the methanol yield increased due to the addition of C_3N_4.

It is also found that methanol yields on Cu-MOR-IE are similar with and without visible light, indicating that Cu-MOR is not photocatalysis for methanol synthesis (Figure S4). Therefore, g-C_3N_4 not only improved the thermal catalytic activity of Cu-MOR but also facilitated the methanol yield under photothermal catalysis.

3. Discussion

3.1. Physical and Chemical Properties Characterizations

To investigate the effect of the preparation method on the structure of the Cu-MOR/g-C_3N_4 composite catalysts, XRD characterization of four catalysts is performed (Figure 2). Figure 2a shows the characteristic peaks of MOR at 9.8°, 13.5°, 19.7°, 22.4°, 25.8°, and 27.7° [37,38]. The SEM images also show that the samples (Figure S5) have the morphology of mercerized zeolite molecular sieve [39]. These results show that the skeleton structure and morphology of MOR unchanged with different preparation methods. The diffraction peaks of copper species are not observed in XRD spectrums of Cu-MOR-IE and Cu-MOR-IM due to the high dispersion of copper species within the MOR channels [40]. However, Cu-MOR-GR and Cu-MOR-HT exhibit a characteristic diffraction peak of CuO at 38.8° [41]. Previous studies have shown that CuO nanoparticles with large particle sizes do not function as active centers for methane conversion, and small Cu_xO_y species in the channel of the zeolites are the active sites [42]. Consequently, the methanol yield of Cu-MOR/g-C_3N_4-GR and Cu-MOR/g-C_3N_4-HT have low yields of methanol. No diffraction peak of g-C_3N_4 is detected in four Cu-MOR/g-C_3N_4 catalysts, which indicated that g-C_3N_4 enters the MOR channel. The crystallinity of the four catalysts decreases after recombination with g-C_3N_4, and the weak peak of CuO of Cu-MOR/g-C_3N_4-GR and Cu-MOR/g-C_3N_4-HT becomes indistinct.

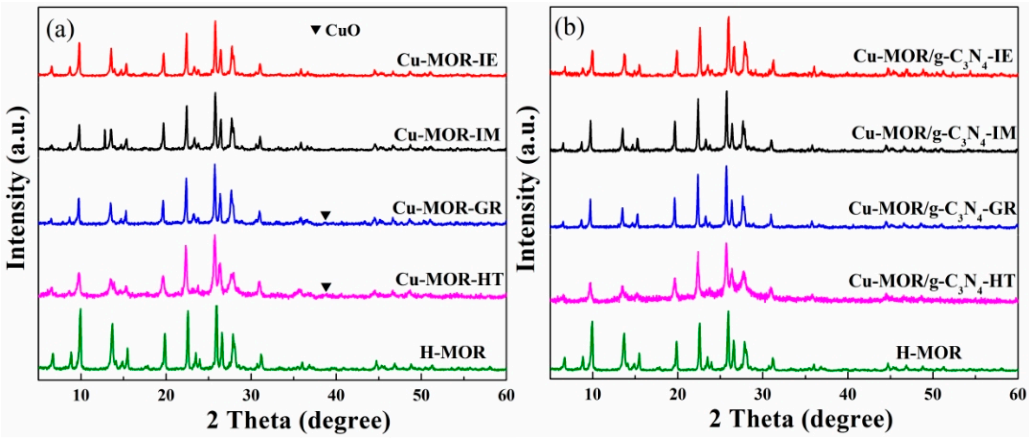

Figure 2. XRD of Cu-MOR (**a**) and Cu-MOR/g-C_3N_4 (**b**) prepared by different methods.

Figure 3 shows the N 1*s* XPS spectra of g-C_3N_4 and Cu-MOR/g-C_3N_4 prepared by different methods. N 1*s* of pure g-C_3N_4 is deconvoluted into two peaks. The first peak at 398.6 eV corresponds to C-N=C groups, and the second peak at 399.8 eV is assigned to N-$(C)_3$ groups [43,44]. Compared to N 1*s* of pure g-C_3N_4, the binding energy of Cu-MOR/g-C_3N_4 shifts to the high binding energy (0.5 eV).

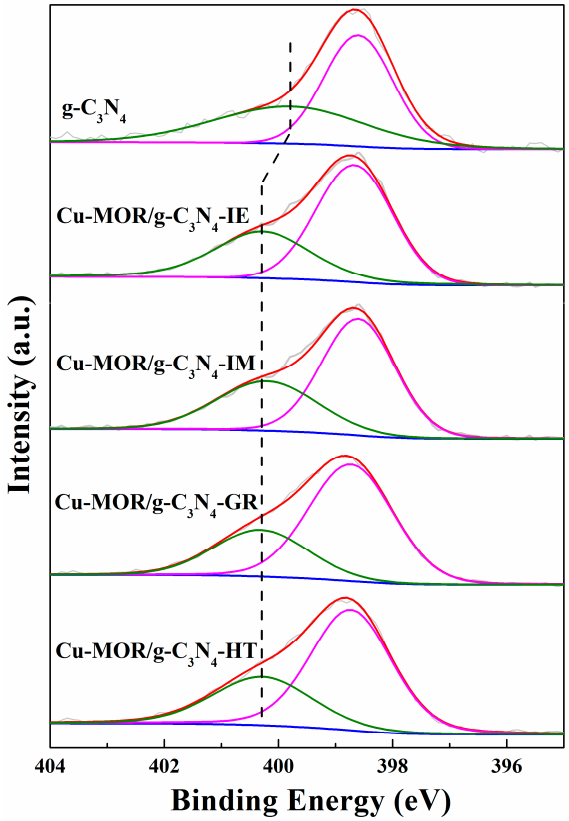

Figure 3. N 1*s* XPS spectrum of g-C_3N_4 and Cu-MOR/g-C_3N_4 prepared by different methods.

For Cu-MOR, the peak at the binding energy of ~933.7 eV represents Cu^{2+} in the channel of the molecular sieve (Figure 4), while the peak at the high binding energy (~935.1 eV) corresponds to hydrated Cu^{2+} [45]. The satellite peaks between ~939.0 and 946.0 eV also verify the existence of Cu^{2+} species. The shapes of satellite peaks are different, showing that the preparation methods affect the characteristics of the Cu species. For Cu-MOR/g-C_3N_4, the satellite peaks disappear, which is absence of hydrated Cu^{2+} due to the high calcination temperature (500 °C) [46–48]. In addition, the peak at ~933.7 eV shifts to low binding energy (~932.1 eV). Thus, the peak at 932.1 eV corresponds to low valence Cu [49]. However, the low content of Cu precludes the observation of Cu LMM peaks, making it impossible to verify the valence of Cu species by XPS. Based on the preparation process, we propose that Cu species is attributed to Cu^{+}. It can be seen that the binding energies of Cu $2p_{3/2}$ (933.7~934.0 eV) of four Cu-MOR/g-C_3N_4 shift to low binding energy (932.1~932.6 eV) compared to Cu-MOR. Combined with the XPS results of N 1*s*, there is an interaction between Cu species and g-C_3N_4, and electrons transfer from g-C_3N_4 to Cu species [50,51].

The relationship between the copper loading of the catalyst and methanol yield is shown in Figure 5 and Table 2. Although Cu-MOR/g-C_3N_4-HT and Cu-MOR/g-C_3N_4-GR have high copper loadings, some Cu species of these two catalysts form CuO nanoparticles outside MOR channels (Figure 2), which are not the active sites for methane activation. Conversely, the Cu-MOR/g-C_3N_4-IE and Cu-MOR/g-C_3N_4-IM catalysts had a low copper content, but most of these Cu species are likely located within the channels of MOR thereby contributing to their relatively high methanol yields. Moreover, according to Groothaert et al. results, a Cu/Al ratio between 0.2 and 0.3 is favorable for methanol synthesis [52], so Cu-MOR/g-C_3N_4-IE with a Cu/Al ratio of 0.23 exhibits the highest methanol yield.

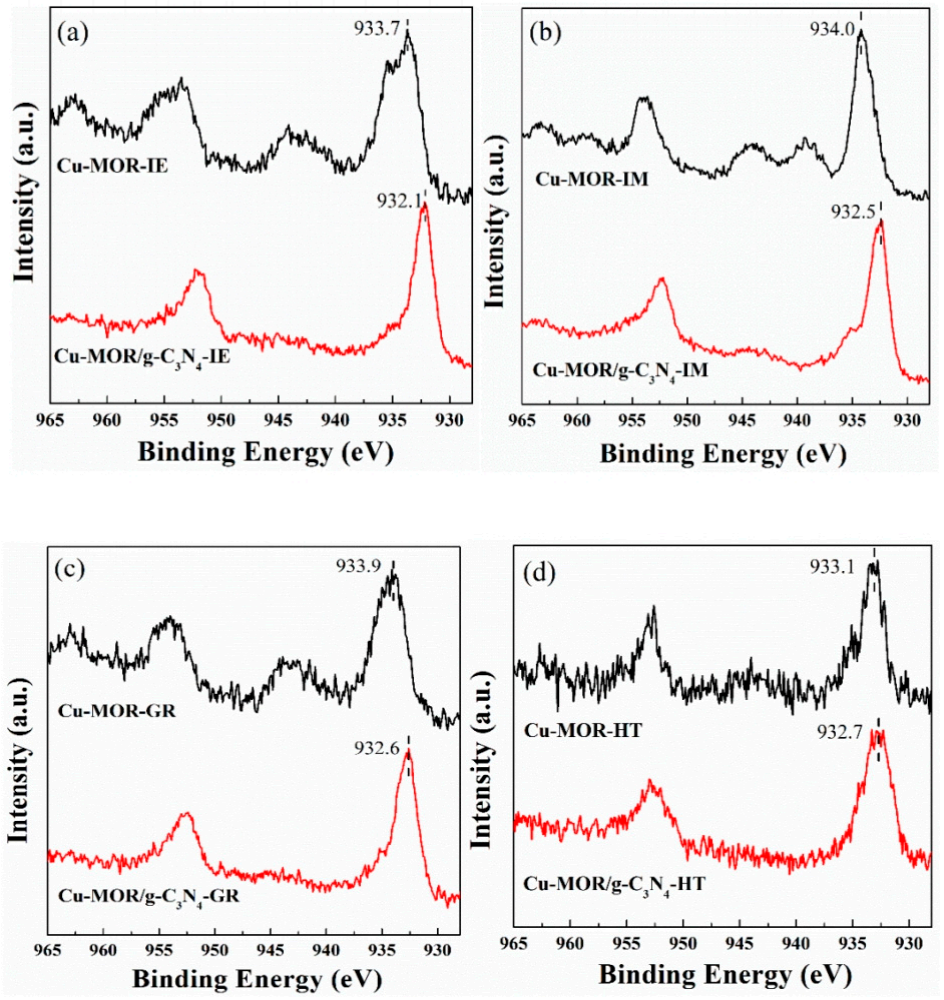

Figure 4. Cu 2*p* XPS spectrum of Cu-MOR and Cu-MOR/g-C_3N_4 prepared by different methods. (**a**) liquid-phase ion exchange; (**b**) isovolumetric impregnation; (**c**) solid-state ion exchange; (**d**) hydrothermal synthesis.

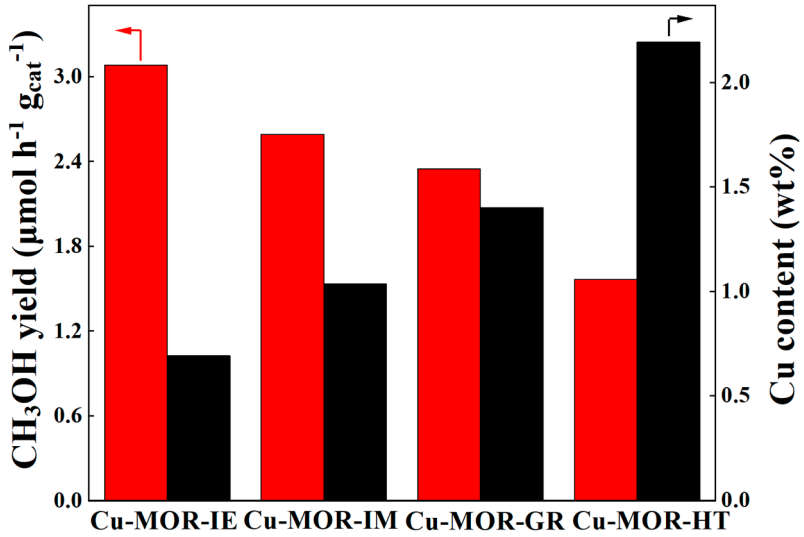

Figure 5. The relationship between copper content and methanol yield of Cu-MOR/g-C_3N_4 prepared by deferent methods.

Table 2. Copper content and Cu/Al of Cu-MOR/g-C_3N_4 with different preparation methods.

Catalyst	Cu Content (wt%)	Cu/Al
Cu-MOR/g-C_3N_4-IE	0.69	0.23
Cu-MOR/g-C_3N_4-IM	1.03	0.32
Cu-MOR/g-C_3N_4-GR	1.40	0.76
Cu-MOR/g-C_3N_4-HT	2.19	1.11

Previous results demonstrate that the N_2 adsorption/desorption isotherms of Cu-MOR are between type I and IV isotherms with a slight secondary uptake [53,54], which contains a large number of micropores and a little mesoporous (type IV isotherms). Conversely, g-C_3N_4 shows a type IV isotherm, reflecting its mesoporous structure [36,55]. When the two materials were combined (Figure 6), the N_2 adsorption/desorption curve failed to close at low pressure, indicating the entry of g-C_3N_4 into the micropores of Cu-MOR. The degree of micropore blockage within Cu-MOR varied depending on the preparation method, while the mesoporous nature of g-C_3N_4 remained constant. The number of micropores increased in the following order Cu-MOR/g-C_3N_4-HT < Cu-MOR/g-C_3N_4-GR < Cu-MOR/g-C_3N_4-IM < Cu-MOR/g-C_3N_4-IE, with the highest degree of pore infiltration observed in Cu-MOR/g-C_3N_4-IE. As the pore content decreased, methanol yield also gradually decreased. The reason is that the feed is difficult to enter the channel and contact with the active site when the pores of MOR are gradually blocked.

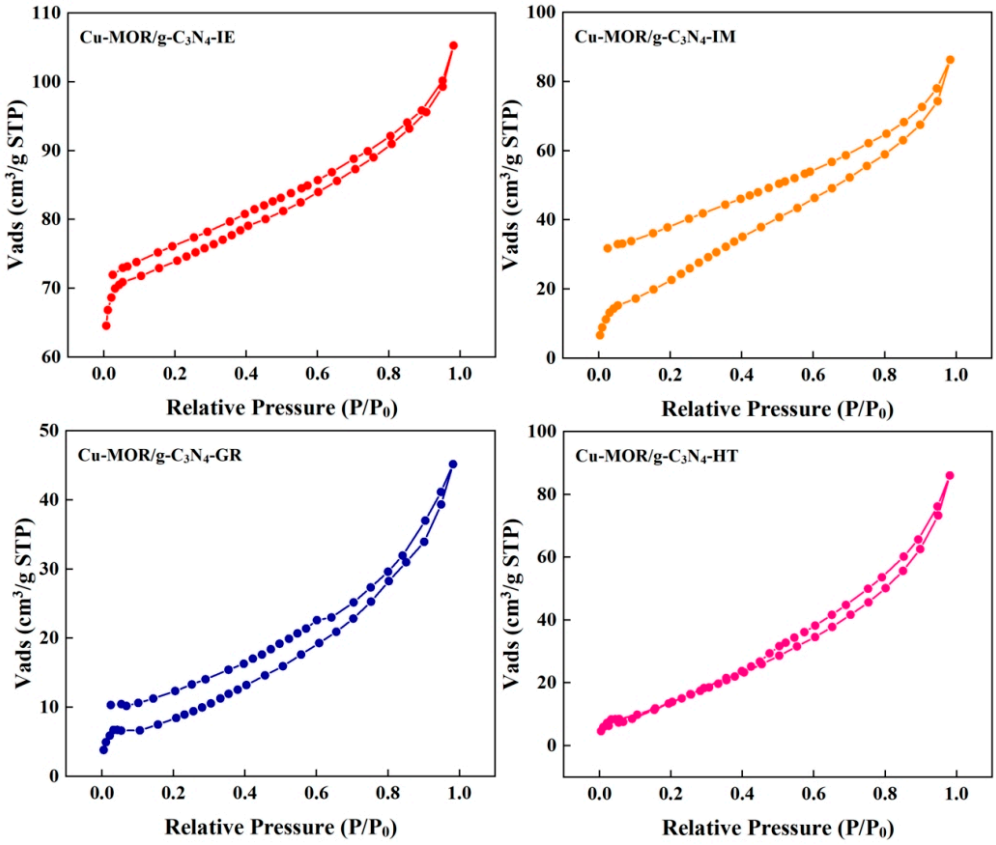

Figure 6. N_2 absorption-desorption isotherms of Cu-MOR/g-C_3N_4 prepared by different methods.

3.2. Photocatalytic Property

Figure 7 is the UV-vis DRS of Cu-MOR/g-C_3N_4 prepared by different methods. All the catalysts have absorption in the visible region. Compared with other catalysts, Cu-MOR/g-C_3N_4-GR shows the strongest broadband absorption owing to the formation of a Z-scheme CuO/g-C_3N_4 heterojunction outside the pore, which enhances light absorption [56,57]. Cu species outside the channels are not the active sites for methane conversion by photothermal

catalysis or thermal catalysis, which explains the lower methanol production rate observed for Cu-MOR/g-C_3N_4-GR compared to that of Cu-MOR/g-C_3N_4-IE and Cu-MOR/g-C_3N_4-IM.

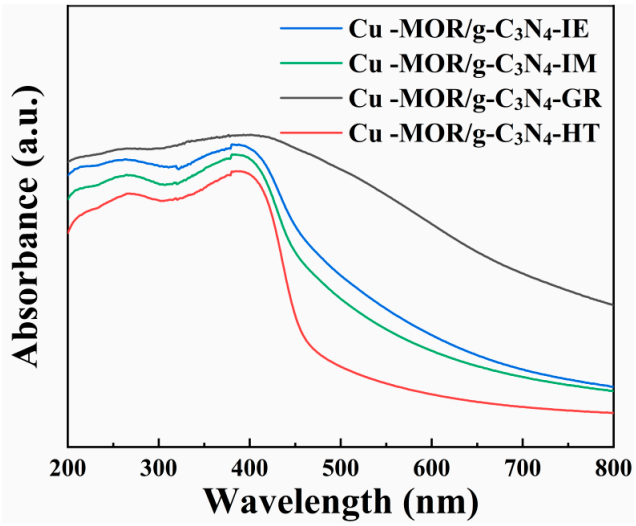

Figure 7. UV-vis DRS of Cu-MOR/g-C_3N_4 prepared by different methods.

EIS is an effective tool to characterize the charge transfer and separation efficiency of photogenerated charge carriers in photocatalysis [58]. Cu-MOR/g-C_3N_4 prepared by different methods is characterized by EIS (Figure 8). The interfacial charge transfer resistances (R_{ct}) in Table S1 are fitted from Nyquist plots using the equivalent circuit model in Zview software. It is found that the sequence of R_{ct} is as follows: Cu-MOR/g-C_3N_4-IE < Cu-MOR/g-C_3N_4-IM < Cu-MOR/g-C_3N_4-GR < Cu-MOR/g-C_3N_4-HT. This order generally reflects the synergy efficiency between photothermal effects and photocatalytic performance. Specifically, lower R_{ct} values indicate a higher charge transfer efficiency and better separation of electron-hole pairs [59,60]. Consequently, a smaller R_{ct} is advantageous for achieving a higher methanol yield.

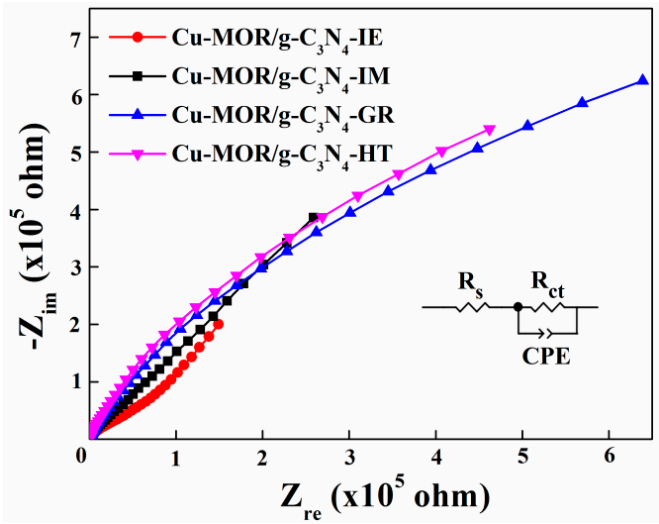

Figure 8. Nyquist plot of Cu-MOR/g-C_3N_4 prepared by different methods.

The PL spectrum shown in Figure 9 illustrates the photoluminescence spectra of Cu-MOR/g-C_3N_4 prepared by different preparation methods, the excitation wavelength is 270 nm. All of the catalysts exhibit strong PL intensity with a peak center of ~458 nm. A lower peak in the PL spectrum indicates a higher separation efficiency of photo-generated electrons and holes. However, it should be pointed out that the PL spectral peak of the catalyst prepared by the solid-state ion exchange method was the lowest, it did not match

the EIS results. Based on the Kasha rule [61], non-radiative recombination dominates the recombination of photogenerated charges and holes in Cu-MOR/g-C_3N_4-GR.

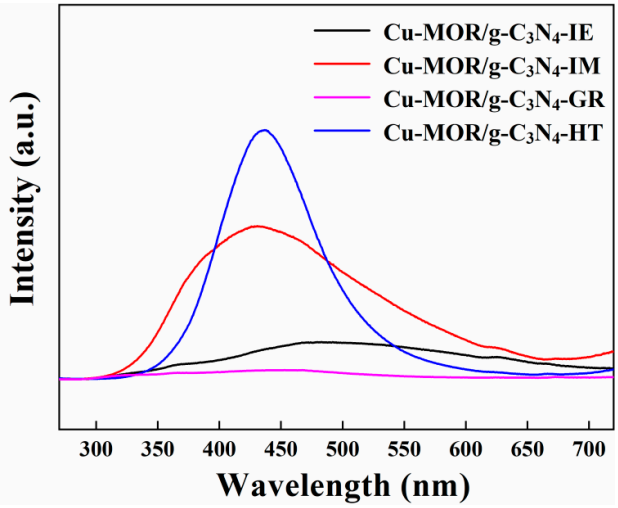

Figure 9. PL spectra of Cu-MOR/g-C_3N_4 with different preparation methods.

3.3. Thermal and Photothermal Mechanism

g-C_3N_4 reduces O_2 to $\cdot O_2^-$ by photothermal catalysis [36]. Subsequently, this $\cdot O_2^-$ species is transferred from g-C_3N_4 to Cu_xO_{y-1}. The formation of active sites in Cu_xO_y species occurs from the oxidation of Cu_xO_{y-1} species using $O_2/\cdot O_2^-$ as the oxidant. Finally, methanol is observed through methane activation and stream extraction. However, Cu-MOR/g-C_3N_4-GR and Cu-MOR/g-C_3N_4-HT contain large particles of CuO, which is not the active site for methane conversion, unlike Cu-MOR/g-C_3N_4-IE and Cu-MOR/g-C_3N_4-IM. Moreover, the preparation methods have significant consequences on the number of micro-pores present in Cu-MOR/g-C_3N_4. As the content of pores decreases, it becomes increasingly difficult for the feed to enter the channels and interact with the active site, leading to a decline in methanol production (Figure 10).

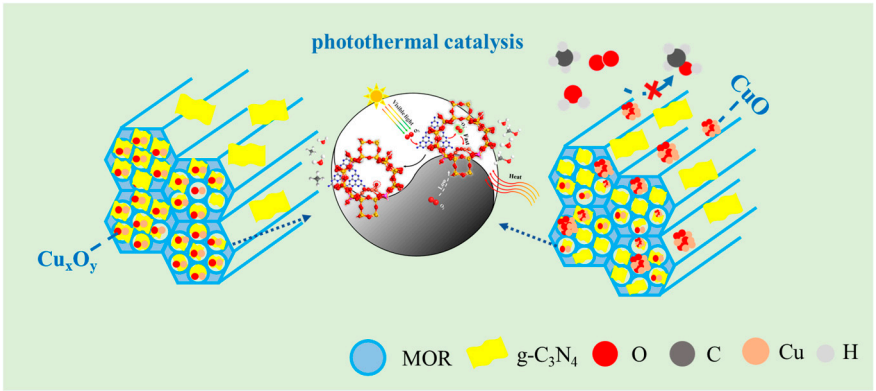

Figure 10. Schematic of direct methanol oxidation synthesis from methane at photothermal catalysis on Cu-MOR/g-C_3N_4 prepared by different preparation methods.

4. Materials and Methods

4.1. Materials

All chemicals used were of analytical grade and were used as received without any further purification. The main materials used in this study were melamine (analytical pure, Aladdin, Shanghai, China), copper acetate (analytical pure, Tianjin Guangfu Technology Development Co., Ltd., Tianjin, China), mercerized zeolite (NH_4-MOR, Si/Al = 25, Nankai University, Tianjin, China), acid silica sols (30%, Qingdao Haiyangchem Co., Ltd., Shandong, China), sodium aluminate (analytical pure, Aladdin, Shanghai, China), sodium hydroxide

(analytical pure, Aladdin, Shanghai, China) and tetramethylammonium hydroxide (35%, analytical pure, Aladdin, Shanghai, China).

4.2. Preparation of the Catalysts

Cu-MOR was prepared by liquid phase ion exchange (IE) [13,47], isovolumetric impregnation(IM) [62], solid-state ion exchange(GR) [63], and hydrothermal synthesis(HT) [64]. which was named as Cu-MOR-IE, Cu-MOR-IM, Cu-MOR-GR and Cu-MOR-HT, respectively. The preparation method is as follows:

Liquid phase ion exchange: The NH_4-MOR was placed in a muffle furnace and calcined in an air atmosphere at 500 °C for 8 h at a heating rate of 2 °C/min to obtain H-MOR; H-MOR was ion-exchanged with 0.01 M of $Cu(CH_3COO)_2$ solution for 24 h at room temperature, and the pH of the solution is controlled at 5.2~5.7 (adjust with ammonia 1 M). The samples were repeatedly washed and centrifuged with deionized water and finally dried at 80 °C for 12 h to obtain Cu-MOR-IE blue powder.

Isovolumetric impregnation: The preparation of H-MOR is consistent with the above method; The $Cu(CH_3COO)_2$ (0.01 M) solution was added drop by drop into H-MOR until $Cu(CH_3COO)_2$ solution could not be absorbed. After dropping, it was left at room temperature for 24 hours, and then vacuum-dried at 60 °C for 4 hours.

Solid-state ion exchange: The preparation of H-MOR was consistent with the above method; Equal masses of H-MOR and $Cu(CH_3COO)_2{\cdot}H_2O$ powder was added to the mortar., mix and grind them to be uniform, then calcined in a muffle furnace at a heating rate of 2 °C/min in an air atmosphere at 500 °C for 8 hours to obtain Cu-MOR-GR blue powder.

Hydrothermal synthesis: Dissolve NaOH in deionized water, then add $NaAlO_2$ and TEAOH then stir the above mixed solution for 30 min. When the solution was clarified, the acid silica sol was added drop by drop under vigorous agitation. After stirring for 30 min, $Cu(CH_3COO)_2$ (0.01 M) solution was added and stirred for 30 min. The above-mixed solution was aged at room temperature for 4 h, and then the solution was transferred to a 120 mL Teflon-lined autoclave and treated at 180 °C for 72 h. The samples were repeatedly washed and centrifuged with deionized water and dried at 80 °C for 12 h, finally, the sample was placed in a muffle furnace and calcined at a heating rate of 2 °C/min in an air atmosphere at 500 °C for 8 h to obtain Cu-MOR-HT blue powder.

Preparation of Cu-MOR/g-C_3N_4: Cu-MOR and melamine were dissolved in a certain ratio in 70 mL deionized water, stirred vigorously at 60 °C for 1 h, then transferred to a 100 mL Teflon-lined autoclave, and treated at 180 °C for 8 h. After washing and centrifugation with deionized water, the samples were dried at 80 °C for 12 h and then calcined at 500 °C for 2.5 h under N_2 atmosphere at a heating rate of 2.5 °C/min to obtain Cu-MOR/g-C_3N_4 powder [65]. Four composite catalysts of Cu-MOR/g-C_3N_4 were named Cu-MOR/g-C_3N_4-IE, Cu-MOR/g-C_3N_4-IM, Cu-MOR/g-C_3N_4-GR and Cu-MOR/g-C_3N_4-HT.

4.3. Activity Test

0.1 g of catalysts were placed in a fixed reactor tube with an inner diameter of 6 mm and length of 450 mm. The catalyst was heated to 500 °C at a ramp rate of 10 °C/min under N_2 atmosphere. Then catalyst was activated at an activation temperature of 500 °C by passing O_2. Afterward, $CH_4/O_2/H_2O$ was introduced into the reaction at a reaction temperature of 200 °C, 1 atm and a ratio of 24/3/8. A 300 W Xeon lamp (CELHXF300-(T3), Aulight, Beijing, China) with suitable filters were used to obtain visible light (wavelength greater than 420 nm). The liquid products were detected using a gas chromatograph (Agilent 7890B, Santa Clara, USA) equipped with a flame ionization detector. The yield of the product was calculated as follows:

$$\mathrm{Yi} = \frac{\mathrm{Pi} \times \mathrm{V}}{\mathrm{Mi} \times \mathrm{mcat}}$$

where Y_i, P_i, V, M_i and m_{cat} were the yield of component i, the mass concentration of component i, the volume of liquid phase received per hour, the molar mass of component i and mass of catalyst.

$$\text{Percentage} = \frac{\text{Yield}_{\text{photo}-\text{thermal}} - \text{Yield}_{\text{thermal}}}{\text{Yield}_{\text{thermal}}}$$

where $\text{Yield}_{\text{photo-thermal}}$ and $\text{Yield}_{\text{thermal}}$ were photothermal catalytic methanol yield and thermal catalytic methanol Yield.

4.4. Catalyst Characterization

The X-ray diffraction (XRD) patterns were characterized by an X-ray diffractometer (MiniFlex‖ Rigaku, Tokyo, Japan) in the 2θ range of 5°–60° with Cu-Kα radiation (λ = 1.5418 Å, 40 kV and 40 mA). The step size was 0.02° and the scan rate was 8°/min. The samples were analyzed for physical and structural analysis using Jade software. The Brunauer–Emmett-Teller (BET) surface areas of the samples were measured with a physical adsorptiometer (NOVA 2000e Quantachrome, Boynton Beach, FL, USA) at −196 °C, using liquid nitrogen as adsorbent. Before the measurement, the samples were pretreated in a vacuum at 300 °C for 6 h. To characterize the morphology of the obtained samples, scanning electron microscopy (SEM) images were collected using a microscope (SU8010 Hitachi, Tokyo, Japan). The powder sample was ground before testing, then glued to a conductive adhesive and sprayed with gold to increase conductivity. X-ray photoelectron spectroscopy (XPS) measurements were performed at ESCALAB 250 (Thermo Fisher Scientific, Waltham, MA, USA), and all the XPS spectra were calibrated by C 1*s* at 284.6 eV. UV–Vis diffuse reflection spectroscopy (UV–Vis DRS) was performed on a PerkinElmer LAMBDA650 spectrophotometer using $BaSO_4$ as the reference material. The content of elements in the sample was tested by ICP-OES (Agilent 7700, Santa Clara, CA, USA). For the test, first dilute the sample with 20 mL aqua regia, then heat the solution at 200 °C for 120 min to fully dissolve the sample and finally dilute it to 50 mL with distilled water. The electrochemical impedance spectroscopy (EIS) measurement was carried out at 25 °C in a standard three-electrode system using an Ag/AgCl electrode and a platinum sheet electrode as reference and counter electrode, a glassy carbon electrode coated with catalyst as working electrode and a 0.5 mol/L Na_2SO_4 solution as electrolyte. The EIS was performed in the frequency range of 0.1 Hz to 10^6 Hz with an applied AC voltage of 5 mV. A total of 8 mg catalyst was added to 180 μL of deionized water, 200 μL of ethanol and 20 μL of 0.5 wt% Nafion solution. An amount of 15 μL of the slurry was applied dropwise to the pre-treated wave carbon electrode after 30 min of sonication and dried at room temperature. The photoluminescence (PL) spectroscopy was investigated by using an RF-6000 (Shimadzu, Kyoto, Japan) and excited with a 270 nm laser.

5. Conclusions

The present study investigates the influences of various preparation methods including liquid phase ion exchange, isovolumetric impregnation, solid-state ion exchange, and hydrothermal synthesis, on the catalytic performance of Cu-MOR/g-C_3N_4 for the direct methanol synthesis from methane oxidation by photothermal catalysis. The correlation between their catalytic activity and several characterization techniques was analyzed. Cu-MOR/g-C_3N_4 prepared by the liquid phase ion exchange method exhibits the best catalytic activity (3.09 μmol h^{-1} $gcat^{-1}$) and excellent stability during 9 h at 200 °C under visible light. The photothermal efficiency for methanol yield on the four catalysts was ranked in the order of Cu-MOR/g-C_3N_4-IE > Cu-MOR/g-C_3N_4-IM > Cu-MOR/g-C_3N_4-GR > Cu-MOR/g-C_3N_4-HT, while Cu-MOR/g-C_3N_4-IE displays the highest photothermal catalytic synergistic effect. XPS and EIS results confirm that the strong interaction between Cu_xO_y species and g-C_3N_4, and small interfacial charge transfer resistance were in favor of methanol yield. Additionally, BET results reveal that excessive g-C_3N_4 blocked the channels of MOR, impeding the active site's exposure to the feed, and eventually leading

to decreased methanol yield. Therefore, it is evident that the structural features of Cu-MOR/g-C_3N_4 and the preparation method impact the catalytic performance. This work provides insights into the understanding and preparation of Cu-MOR/g-C_3N_4 as a high-performance photothermal catalyst using different methods.

Supplementary Materials: The following supporting information can be downloaded at: https://www.mdpi.com/article/10.3390/catal13050868/s1, Figure S1: Methanol yield of Cu-MOR/g-C_3N_4 prepared by different methods by photothermal catalysis and thermal catalysis; Figure S2: CH_3OH yield on Cu-MOR/g-C_3N_4-IE by photo catalysis; Figure S3: Methanol yield of Cu-MOR prepared by different methods by thermal catalysis; Figure S4: Methanol yield of Cu-MOR-IE by photothermal catalysis and thermal catalysis; Figure S5: SEM of Cu-MOR/g-C_3N_4 with different preparation methods; Table S1: Fitted EIS results of Cu-MOR/g-C_3N_4 with different preparation methods based on the equivalent circuit.

Author Contributions: Conceptualization and project administration, Z.-J.Z. and Z.-X.Z.; methodology, J.-C.H., M.R. and J.-X.Z.; formal analysis, M.R., R.-X.Z. and Z.-H.G., writing—original draft preparation, J.-C.H., R.-X.Z. and J.-X.Z.; writing—review and editing, R.-X.Z. and Z.-H.G.; funding acquisition, L.L. and Z.-X.Z. All authors have read and agreed to the published version of the manuscript.

Funding: The authors would like to thank the National Natural Science Foundation of China (No. 22078214 and U1910202), Special fund for Science and Technology Innovation Team of Shanxi Province (No. 202204051001009), Central Government Guides the Local Science and Technology Development Special Fund (No. YDZJSX2022A013), Special Project of Science and Technology Cooperation and Exchange of Shanxi Province (No. 202204041101011) and the Scientific, and Technological Key Project of Industrial Research of JinZhong (Y211018) for their financial support.

Data Availability Statement: Not applicable.

Conflicts of Interest: The authors declare no conflict of interest.

References

1. Konno, Y.; Fujii, T.; Sato, A.; Akamine, K.; Naiki, M.; Masuda, Y.; Yamamoto, K.; Nagao, J. Key Findings of the World's First Offshore Methane Hydrate Production Test off the Coast of Japan: Toward Future Commercial Production. *Energy Fuels* **2017**, *31*, 2607–2616. [CrossRef]
2. Mahyuddin, M.H.; Shiota, Y.; Yoshizawa, K. Methane selective oxidation to methanol by metal-exchanged zeolites: A review of active sites and their reactivity. *Catal. Sci. Technol.* **2019**, *9*, 1744–1768. [CrossRef]
3. McFarland, E. Unconventional Chemistry for Unconventional Natural Gas. *Science* **2012**, *338*, 340–342. [CrossRef]
4. Moore, T.A. Coalbed methane: A review. *Int. J. Coal Geol.* **2012**, *101*, 36–81. [CrossRef]
5. Wu, L.; Fan, W.; Wang, X.; Lin, H.; Tao, J.; Liu, Y.; Deng, J.; Jing, L.; Dai, H. Methane Oxidation over the Zeolites-Based Catalysts. *Catalysts* **2023**, *13*, 604. [CrossRef]
6. Yu, C.; Shen, S. Progress in studies of natural gas conversion in China. *Pet. Sci.* **2008**, *5*, 67–72. [CrossRef]
7. Han, P.; Zhang, Z.; Chen, Z.; Lin, J.; Wan, S.; Wang, Y.; Wang, S. Critical Role of Al Pair Sites in Methane Oxidation to Methanol on Cu-Exchanged Mordenite Zeolites. *Catalysts* **2021**, *11*, 751. [CrossRef]
8. Tao, L.; Lee, I.-W.; Sanchez-Sanchez, M. Cu oxo nanoclusters for direct oxidation of methane to methanol: Formation, structure and catalytic performance. *Catal. Sci. Technol.* **2020**, *10*, 7124–7141. [CrossRef]
9. Sirajuddin, S.; Rosenzweig, A.C. Enzymatic oxidation of methane. *Biochemistry* **2015**, *54*, 2283–2294. [CrossRef]
10. Zhou, C.; Li, S.; He, S.; Zhao, Z.; Jiao, Y.; Zhang, H. Temperature-dependant active sites for methane continuous conversion to methanol over Cu-zeolite catalysts using water as the oxidant. *Fuel* **2022**, *329*, 125483. [CrossRef]
11. Wulfers, M.J.; Teketel, S.; Ipek, B.; Lobo, R.F. Conversion of methane to methanol on copper-containing small-pore zeolites and zeotypes. *ChemComm* **2015**, *51*, 4447–4450. [CrossRef] [PubMed]
12. Tomkins, P.; Mansouri, A.; Bozbag, S.E.; Krumeich, F.; Park, M.B.; Alayon, E.M.; Ranocchiari, M.; van Bokhoven, J.A. Isothermal Cyclic Conversion of Methane into Methanol over Copper-Exchanged Zeolite at Low Temperature. *Angew. Chem. Int. Ed.* **2016**, *55*, 5467–5471. [CrossRef] [PubMed]
13. Grundner, S.; Markovits, M.A.C.; Li, G.; Tromp, M.; Pidko, E.A.; Hensen, E.J.M.; Jentys, A.; Sanchez-Sanchez, M.; Lercher, J.A. Single-site trinuclear copper oxygen clusters in mordenite for selective conversion of methane to methanol. *Nat. Commun.* **2015**, *6*, 7546. [CrossRef] [PubMed]
14. Bao, J.; Yang, G.; Yoneyama, Y.; Tsubaki, N. Significant Advances in C1 Catalysis: Highly Efficient Catalysts and Catalytic Reactions. *ACS Catal.* **2019**, *9*, 3026–3053. [CrossRef]

15. Koo, C.W.; Rosenzweig, A.C. Biochemistry of aerobic biological methane oxidation. *Chem. Soc. Rev.* **2021**, *50*, 3424–3436. [CrossRef]
16. Eid, K.; Gamal, A.; Abdullah, A.M. Graphitic carbon nitride-based nanostructures as emergent catalysts for carbon monoxide (CO) oxidation. *Green Chem.* **2023**, *25*, 1276–1310. [CrossRef]
17. Xie, P.; Ding, J.; Yao, Z.; Pu, T.; Zhang, P.; Huang, Z.; Wang, C.; Zhang, J.; Zecher-Freeman, N.; Zong, H.; et al. Oxo dicopper anchored on carbon nitride for selective oxidation of methane. *Nat. Commun.* **2022**, *13*, 1375. [CrossRef]
18. Eid, K.; Sliem, M.H.; Al-Ejji, M.; Abdullah, A.M.; Harfouche, M.; Varma, R.S. Hierarchical Porous Carbon Nitride-Crumpled Nanosheet-Embedded Copper Single Atoms: An Efficient Catalyst for Carbon Monoxide Oxidation. *ACS Appl. Mater. Interfaces* **2022**, *14*, 40749–40760. [CrossRef]
19. Eid, K.; Sliem, M.H.; Al-Kandari, H.; Sharaf, M.A.; Abdullah, A.M. Rational Synthesis of Porous Graphitic-like Carbon Nitride Nanotubes Codoped with Au and Pd as an Efficient Catalyst for Carbon Monoxide Oxidation. *Langmuir* **2019**, *35*, 3421–3431. [CrossRef]
20. Narsimhan, K.; Iyoki, K.; Dinh, K.; Román-Leshkov, Y. Catalytic Oxidation of Methane into Methanol over Copper-Exchanged Zeolites with Oxygen at Low Temperature. *ACS Cent. Sci.* **2016**, *2*, 424–429. [CrossRef]
21. Dinh, K.T.; Sullivan, M.M.; Narsimhan, K.; Serna, P.; Meyer, R.J.; Dincă, M.; Román-Leshkov, Y. Continuous Partial Oxidation of Methane to Methanol Catalyzed by Diffusion-Paired Copper Dimers in Copper-Exchanged Zeolites. *J. Am. Chem. Soc.* **2019**, *141*, 11641–11650. [CrossRef] [PubMed]
22. Sun, L.; Wang, Y.; Wang, C.; Xie, Z.; Guan, N.; Li, L. Water-involved methane-selective catalytic oxidation by dioxygen over copper zeolites. *Chem* **2021**, *7*, 1557–1568. [CrossRef]
23. Song, C.; Wang, Z.; Yin, Z.; Xiao, D.; Ma, D. Principles and applications of photothermal catalysis. *Chem. Catal.* **2022**, *2*, 52–83. [CrossRef]
24. Wei, L.; Yu, C.; Yang, K.; Fan, Q.; Ji, H. Recent advances in VOCs and CO removal via photothermal synergistic catalysis. *Chin. J. Catal.* **2021**, *42*, 1078–1095. [CrossRef]
25. Mateo, D.; Cerrillo, J.L.; Durini, S.; Gascon, J. Fundamentals and applications of photo-thermal catalysis. *Chem. Soc. Rev.* **2021**, *50*, 2173–2210. [CrossRef]
26. Han, L.; Mao, J.; Xie, A.-Q.; Liang, Y.; Zhu, L.; Chen, S. Synergistic enhanced solar-driven water purification and CO_2 reduction via photothermal catalytic membrane distillation. *Sep. Purif. Technol.* **2023**, *309*, 123003. [CrossRef]
27. Cai, M.; Wu, Z.; Li, Z.; Wang, L.; Sun, W.; Tountas, A.A.; Li, C.; Wang, S.; Feng, K.; Xu, A.-B.; et al. Greenhouse-inspired supra-photothermal CO_2 catalysis. *Nat. Energy* **2021**, *6*, 807–814. [CrossRef]
28. Guo, S.; Li, X.; Li, J.; Wei, B. Boosting photocatalytic hydrogen production from water by photothermally induced biphase systems. *Nat. Commun.* **2021**, *12*, 1343. [CrossRef]
29. Lu, J.; Shi, Y.; Chen, Z.; Sun, X.; Yuan, H.; Guo, F.; Shi, W. Photothermal effect of carbon dots for boosted photothermal-assisted photocatalytic water/seawater splitting into hydrogen. *Chem. Eng. J.* **2023**, *453*, 139834. [CrossRef]
30. Song, H.; Ye, J. Photothermal tandem catalysis for CO_2 hydrogenation to methanol. *Chem* **2022**, *8*, 1181–1183. [CrossRef]
31. Du, R.; Zhu, H.; Zhao, H.; Lu, H.; Dong, C.; Liu, M.; Yang, F.; Yang, J.; Wang, J.; Pan, J. Modulating photothermal properties by integration of fined Fe–Co in confined carbon layer of SiO_2 nanosphere for pollutant degradation and solar water evaporation. *Environ. Res.* **2023**, *222*, 115365. [CrossRef] [PubMed]
32. Zhang, G.; Liu, J.; Xu, Y.; Sun, Y. A review of CH_4-CO_2 reforming to synthesis gas over Ni-based catalysts in recent years (2010–2017). *Int. J. Hydrog. Energy* **2018**, *43*, 15030–15054. [CrossRef]
33. Marinković, M.; Waisi, H.; Blagojević, S.; Zarubica, A.; Ljupković, R.; Krstić, A.; Janković, B. The effect of process parameters and catalyst support preparation methods on the catalytic efficiency in transesterification of sunflower oil over heterogeneous KI/Al_2O_3-based catalysts for biodiesel production. *Fuel* **2022**, *315*, 123246. [CrossRef]
34. Han, M.-J.; Jiao, Y.-L.; Zhou, C.-H.; Guo, Y.-L.; Guo, Y.; Lu, G.-Z.; Wang, L.; Zhan, W.-C. Catalytic activity of Cu–SSZ-13 prepared with different methods for NH_3-SCR reaction. *Rare Metals* **2019**, *38*, 210–220. [CrossRef]
35. Nguyen, T.H.; Kim, H.B.; Park, E.D. CO and CO_2 Methanation over CeO_2-Supported Cobalt Catalysts. *Catalysts* **2022**, *12*, 212. [CrossRef]
36. Chen, Y.-Q.; Zhang, R.-X.; Ren, M.; Jin, Y.-X.; Wang, W.-J.; Feng, J.-Y.; Gao, Z.-H.; Yan, Z.-F.; Liu, Y.-M.; Huang, W.; et al. Photo-assisted thermal catalysis for methanol synthesis from methane oxidation on Cu-MOR/g-C_3N_4. *Fuel* **2023**, *340*, 127525. [CrossRef]
37. Al-Rawi, U.A.; Sher, F.; Hazafa, A.; Bilal, M.; Lima, E.C.; Al-Shara, N.K.; Jubeen, F.; Shanshool, J. Synthesis of Zeolite supported bimetallic catalyst and application in n-hexane hydro-isomerization using supercritical CO_2. *J. Environ. Chem. Eng.* **2021**, *9*, 105206. [CrossRef]
38. Al-Rawi, U.A.; Sher, F.; Hazafa, A.; Rasheed, T.; Al-Shara, N.K.; Lima, E.C.; Shanshool, J. Catalytic Activity of Pt Loaded Zeolites for Hydroisomerization of n-Hexane Using Supercritical CO_2. *Ind. Eng. Chem. Res.* **2020**, *59*, 22092–22106. [CrossRef]
39. Tavolaro, A.; Riccio, I.I.; Tavolaro, P. Hydrothermal synthesis of zeolite composite membranes and crystals as potential vectors for drug-delivering biomaterials. *Microporous Mesoporous Mater.* **2013**, *167*, 62–70. [CrossRef]
40. Zhan, H.; Huang, S.; Li, Y.; Lv, J.; Wang, S.; Ma, X. Elucidating the nature and role of Cu species in enhanced catalytic carbonylation of dimethyl ether over Cu/H-MOR. *Catal. Sci. Technol.* **2015**, *5*, 4378–4389. [CrossRef]

41. Zhang, W.; Xie, J.; Hou, W.; Liu, Y.; Zhou, Y.; Wang, J. One-Pot Template-Free Synthesis of Cu–MOR Zeolite toward Efficient Catalyst Support for Aerobic Oxidation of 5-Hydroxymethylfurfural under Ambient Pressure. *ACS Appl. Mater. Interfaces* **2016**, *8*, 23122–23132. [CrossRef] [PubMed]
42. Fu, L.; Yuan, M.; Li, X.; Bian, S.; Mi, L.; Gao, Z.; Shi, Q.; Huang, W.; Zuo, Z. The Influence of UiO-bpy Skeleton for the Direct Methane-to-Methanol Conversion on Cu@UiO-bpy: Importance of the Encapsulation Effect. *ChemCatChem* **2021**, *13*, 4897–4902. [CrossRef]
43. Chen, P.; Dong, F.; Ran, M.; Li, J. Synergistic photo-thermal catalytic NO purification of MnO_x/g-C_3N_4: Enhanced performance and reaction mechanism. *Chin. J. Catal.* **2018**, *39*, 619–629. [CrossRef]
44. Tong, Z.; Yang, D.; Shi, J.; Nan, Y.; Sun, Y.; Jiang, Z. Three-Dimensional Porous Aerogel Constructed by g-C_3N_4 and Graphene Oxide Nanosheets with Excellent Visible-Light Photocatalytic Performance. *ACS Appl. Mater. Interfaces* **2015**, *7*, 25693–25701. [CrossRef]
45. Sainz-Vidal, A.; Balmaseda, J.; Lartundo-Rojas, L.; Reguera, E. Preparation of Cu–mordenite by ionic exchange reaction under milling: A favorable route to form the mono-(μ-oxo) dicopper active species. *Microporous Mesoporous Mater.* **2014**, *185*, 113–120. [CrossRef]
46. Pappas, D.K.; Borfecchia, E.; Dyballa, M.; Pankin, I.A.; Lomachenko, K.A.; Martini, A.; Signorile, M.; Teketel, S.; Arstad, B.; Berlier, G.; et al. Methane to Methanol: Structure–Activity Relationships for Cu-CHA. *J. Am. Chem. Soc.* **2017**, *139*, 14961–14975. [CrossRef]
47. Kim, Y.; Kim, T.Y.; Lee, H.; Yi, J. Distinct activation of Cu-MOR for direct oxidation of methane to methanol. *ChemComm* **2017**, *53*, 4116–4119. [CrossRef]
48. Markovits, M.A.C.; Jentys, A.; Tromp, M.; Sanchez-Sanchez, M.; Lercher, J.A. Effect of Location and Distribution of Al Sites in ZSM-5 on the Formation of Cu-Oxo Clusters Active for Direct Conversion of Methane to Methanol. *Top. Catal.* **2016**, *59*, 1554–1563. [CrossRef]
49. Zuo, Z.-J.; Li, J.; Han, P.-D.; Huang, W. XPS and DFT Studies on the Autoxidation Process of Cu Sheet at Room Temperature. *J. Phys. Chem. C* **2014**, *118*, 20332–20345. [CrossRef]
50. You, J.; Bao, W.; Wang, L.; Yan, A.; Guo, R. Preparation, visible light-driven photocatalytic activity, and mechanism of multiphase CdS/C_3N_4 inorganic-organic hybrid heterojunction. *J. Alloys Compd.* **2021**, *866*, 158921. [CrossRef]
51. Zhou, Y.; Zhang, L.; Wang, W. Direct functionalization of methane into ethanol over copper modified polymeric carbon nitride via photocatalysis. *Nat. Commun.* **2019**, *10*, 506. [CrossRef] [PubMed]
52. Groothaert, M.H.; Smeets, P.J.; Sels, B.F.; Jacobs, P.A.; Schoonheydt, R.A. Selective Oxidation of Methane by the Bis(μ-oxo)dicopper Core Stabilized on ZSM-5 and Mordenite Zeolites. *J. Am. Chem. Soc.* **2005**, *127*, 1394–1395. [CrossRef] [PubMed]
53. Tan, F.; Liu, M.; Li, K.; Wang, Y.; Wang, J.; Guo, X.; Zhang, G.; Song, C. Facile synthesis of size-controlled MIL-100(Fe) with excellent adsorption capacity for methylene blue. *Chem. Eng. J.* **2015**, *281*, 360–367. [CrossRef]
54. Férey, G.; Serre, C.; Mellot-Draznieks, C.; Millange, F.; Surblé, S.; Dutour, J.; Margiolaki, I. A Hybrid Solid with Giant Pores Prepared by a Combination of Targeted Chemistry, Simulation, and Powder Diffraction. *Angew. Chem. Int. Ed.* **2004**, *43*, 6296–6301. [CrossRef]
55. Yang, L.; Ren, X.; Zhang, Y.; Chen, Z.; Wan, J. One-step synthesis of a heterogeneous catalyst: Cu^+-decorated triazine-based g-C_3N_4 nanosheet formation and catalytic mechanism. *J. Environ. Chem. Eng.* **2021**, *9*, 105558. [CrossRef]
56. Wu, X.; Zhao, Q.; Zhang, J.; Li, S.; Liu, H.; Liu, K.; Li, Y.; Kong, D.; Sun, H.; Wu, M. 0D carbon dots intercalated Z-scheme CuO/g-C_3N_4 heterojunction with dual charge transfer pathways for synergetic visible-light-driven photo-Fenton-like catalysis. *J. Colloid Interface Sci.* **2023**, *634*, 972–982. [CrossRef]
57. Mohamed, R.M.; Ismail, A.A. Triblock copolymer-assisted synthesis of Z-scheme porous g-C_3N_4 based photocatalysts with promoted visible-light-driven performance. *Ceram. Int.* **2020**, *46*, 28903–28913. [CrossRef]
58. Wang, R.; Gu, L.; Zhou, J.; Liu, X.; Teng, F.; Li, C.; Shen, Y.; Yuan, Y. Quasi-Polymeric Metal–Organic Framework UiO-66/g-C_3N_4 Heterojunctions for Enhanced Photocatalytic Hydrogen Evolution under Visible Light Irradiation. *Adv. Mater. Interfaces* **2015**, *2*, 1500037. [CrossRef]
59. Dai, Z.; Lian, J.; Sun, Y.; Li, L.; Zhang, H.; Hu, N.; Ding, D. Fabrication of g-C_3N_4/Sn_3O_4/Ni electrode for highly efficient photoelectrocatalytic reduction of U(VI). *Chem. Eng. J.* **2022**, *433*, 133766. [CrossRef]
60. Karimi-Nazarabad, M.; Ahmadzadeh, H.; Goharshadi, E.K. Porous perovskite-lanthanum cobaltite as an efficient cocatalyst in photoelectrocatalytic water oxidation by bismuth doped g-C_3N_4. *Sol. Energy* **2021**, *227*, 426–437. [CrossRef]
61. Demchenko, A.P.; Tomin, V.I.; Chou, P.-T. Breaking the Kasha Rule for More Efficient Photochemistry. *Chem. Rev.* **2017**, *117*, 13353–13381. [CrossRef] [PubMed]
62. Beznis, N.V.; Weckhuysen, B.M.; Bitter, J.H. Partial Oxidation of Methane Over Co-ZSM-5: Tuning the Oxygenate Selectivity by Altering the Preparation Route. *Catal. Letters* **2010**, *136*, 52–56. [CrossRef]
63. Le, H.V.; Parishan, S.; Sagaltchik, A.; Göbel, C.; Schlesiger, C.; Malzer, W.; Trunschke, A.; Schomäcker, R.; Thomas, A. Solid-State Ion-Exchanged Cu/Mordenite Catalysts for the Direct Conversion of Methane to Methanol. *ACS Catal.* **2017**, *7*, 1403–1412. [CrossRef]

64. He, P.; Li, Y.; Cai, K.; Xiong, X.; Lv, J.; Wang, Y.; Huang, S.; Ma, X. Nano-Assembled Mordenite Zeolite with Tunable Morphology for Carbonylation of Dimethyl Ether. *ACS Appl. Nano Mater.* **2020**, *3*, 6460–6468. [CrossRef]
65. Wang, Z.; Chen, M.; Huang, Y.; Shi, X.; Zhang, Y.; Huang, T.; Cao, J.; Ho, W.; Lee, S.C. Self-assembly synthesis of boron-doped graphitic carbon nitride hollow tubes for enhanced photocatalytic NO_x removal under visible light. *Appl. Catal. B* **2018**, *239*, 352–361. [CrossRef]